Journal Pre-proof

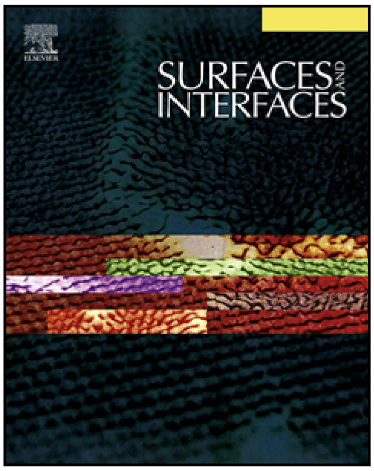

Insights into the role of surface properties on the optical, electronic and nanoparticles morphology of scheelite $BaMoO_4$

José A.S. Laranjeira , Sergio A. Azevedo , Nicolas F. Martins , Felipe A. La Porta , Elson Longo , Julio R. Sambrano

PII: S2468-0230(24)00053-1
DOI: https://doi.org/10.1016/j.surfin.2024.103894
Reference: SURFIN 103894

To appear in: *Surfaces and Interfaces*

Received date: 22 September 2023
Revised date: 23 December 2023
Accepted date: 11 January 2024

Please cite this article as: José A.S. Laranjeira , Sergio A. Azevedo , Nicolas F. Martins , Felipe A. La Porta , Elson Longo , Julio R. Sambrano , Insights into the role of surface properties on the optical, electronic and nanoparticles morphology of scheelite $BaMoO_4$, *Surfaces and Interfaces* (2024), doi: https://doi.org/10.1016/j.surfin.2024.103894

Insights into the role of surface properties on the optical, electronic and nanoparticles morphology of scheelite $BaMoO_4$

José A. S. Laranjeira[1],Sergio A. Azevedo[1,2], Nicolas F. Martins[1], Felipe A. La Porta[3,4] Elson Longo[5], Julio R. Sambrano[1]*

[1]Modeling and Molecular Simulation Group, São Paulo State University (Unesp), Bauru, SP, Brazil

[2] Federal Institute of Maranhão – IFMA, 65950-000, Barra do Corda, MA, Brazil

[3] Nanotechnology and Computational Chemistry Laboratory, Federal University of Technology—Paraná, Londrina 86036-370, PR, Brazil

[4] Post-Graduation Program in Chemistry, State University of Londrina, Londrina 86057-970, PR, Brazil

[5] CDMF-LIEC, UFSCar, P.O. Box 676, São Carlos, SP, 13565-905, Brazil

ABSTRACT

Wide band gap semiconductors, such as barium molybdate ($BaMoO_4$), remain to attract much interest due to their excellent optical, catalytic, and electronic applications. Herein, computational simulations based on the density functional theory (DFT) calculations were carried out to conduct a systematic study of the electronic, structural, and catalytic properties of $BaMoO_4$ bulk and its (001), (112), (101), (110), (103), (100), (111) and (211) surfaces. It was found that the relative stability order (001) > (112) > (101) > (110) > (103) > (100) > (111) > (211). Band gap energies between 2.06 eV (211) and 4.56 eV (101) were observed. The (112) and (103) surfaces are p-type, while the others exhibit characteristics of n-type semiconductors. Additionally, by the band edge alignment analysis, all surfaces are suitable for promoting the O_2 to $^{\bullet}O_2^-$ and the H^+ to H_2 reactions. Finally, a detailed mapping of morphological transformation routes of nano/microstructures was built, contributing experimentalists to frontier research with scheelite-type materials. Therefore, understanding and controlling the morphology allows the development of new materials with highly customized properties and functionality, leading to advances in various fields such as electronics, energy storage and catalysis, among other applications.

Keywords: $BaMoO_4$; scheelite, morphology; DFT; Wulff; electronic transport; catalysis.

1. Introduction

As is known, materials design is an important field of research dedicated to the development of new materials, including nanoparticles (NPs) with their controlled physical and chemical characteristics, e.g., shape, size, structures and atomic/compositional configurations of its most exposed faces, which can significantly impact their properties and applications [1–4]. From this perspective, researchers have reported that the experimental parameters of synthesis (such as time, solvent, temperature, pressure, pH, different reducing agents and surfactants, and so on) may significantly affect the nucleation and growth of these materials, taking to a huge variety of particle shapes and sizes [5–8].

We are currently facing a tremendous global demand to develop novel wide band gap semiconductor materials, which can contribute to the emergence of many high-performance technological applications [9–12]. Among these materials, the barium molybdate ($BaMoO_4$), hereafter named BMO, is a wide band gap (~4.6 eV) semiconductor that crystallizes into a scheelite-type and exhibits interesting physical and chemical properties, including high thermal resistance, optical transparency, and catalytic properties [13,14], which has excellent potential in electro-optics applications [15]. BMO can be synthesized by several routes, including solid-state reaction [16], electrochemical method [17], complex polymerization method [18], reverse microemulsion [19], solvothermal synthesis [20], microwave-assisted hydrothermal [21], coprecipitation [22], and sonochemical method [23]. All these strategies have contributed to finding a huge morphological diversity for $BaMoO_4$ [24–26], which impacts its physical and chemical properties [27,28].

Through computational research it is possible to understand the materials surface-dependent properties at the atomic level with low cost and reduced time, leading to a substantial reduction in time for the emergence of new technologies [29–31]. As is well-known, applying the Wulff theorem [32] allows an easy morphological characterization through the close relation with the relative stability order of the surfaces. It should be noted that the relative stability of the surfaces is obtained by calculating the energy of each surface, which can only be obtained via theoretical methods. Therefore, this consolidated methodology can elucidate the surface structure/composition and predict the final shape of a given material from a materials design perspective [33–37].

Some computational studies have made it possible to reveal a close relationship between the structure and property of the BMO. For instance, Zhao et al. [38] use density functional theory (DFT) [39] simulations to observe that the interstitial oxygen of BMO provokes a visible range absorption band peaked at ~320 nm. Qin et al. [40] explain that the increased electronic density around Mo atoms leads to a BMO dielectric constant decrease under high pressure. Percinatto et al. [41] studied oxygen vacancy in BMO by means of DFT calculations and found the increased hardness of the material, making it more resistant to compression and shear.

Therefore, a systematic computational study of the surface effects on the optical, catalytic, electronic and transport properties of BMO was outlined here. For this purpose, the analysis began with the periodic DFT simulations of the BMO bulk and its (001), (100), (101), (103), (110), (111), (112), and (211) surfaces. In addition, the Wulff construction was used to elaborate a detailed mapping of the morphological nanoparticles transformation. This research is expected to help analyze and predict the experimental results of the BMO and related systems. In this direction, understanding the morphological-dependent properties of BMO can lead to new perspectives and opportunities for its potential technological use in the future.

2. Computational Setup

The electronic and structural properties of BMO bulk and its surfaces were simulated via the periodic DFT approach implemented in the CRYSTAL17 package [42], which expressed the crystalline orbitals regarding Bloch functions. These simulations were conducted with the modified (8 % of the Hartree-Fock (HF) exchange percentage) hybrid B1WC [43], as reported by Sambrano et al. [44]. In addition, the Ba, Mo and O atom centers were described by the 311(1d)G [45], 311(d31)G [46], and 8-411d1 [47] basis set functions, respectively, which are available at the Crystal library (www.crystal.unito.it/basis-sets.php).

For a better description, the geometrical optimization convergence was checked on gradient components and nuclear displacements with tolerances on their root mean square (RMS) set to 0.0001 and 0.0004 a.u., respectively. The precision of the convergence criteria for bi-electronic integrals was controlled by a set of five thresholds (10^{-7}, 10^{-7}, 10^{-7}, 10^{-7}, 10^{-14}) using the TOLINTEG keyword in DFT calculations, representing the overlap and penetration for Coulomb integrals, the overlap for HF exchange integrals, and the pseudo-overlap, respectively. The reciprocal space was sampled with a shrinking factor defined as 8 (SHRINK keyword), corresponding to 78-k-points in the irreducible Brillouin zone (BZ).

The band structure and density of states (DOS) were analyzed using the same k-point sampling employed for the diagonalization of the Fock matrix in the optimization process along the high-symmetry BZ path.

The Raman intensities were computed with the solutions of first and second order coupled perturbed Hartree-Fock/Kohn Sham (CPHF/KS) self-consistent equations [48,49].

3. Model System

Table 1 shows the experimental and standard B1WC and modified B1WC (8%) simulations results for the cell parameters and band gap energy (E_{gap}) calculations. Both functionals yield high accuracy concerning the lattice parameters; nevertheless, compared with the experimental results, greater accuracy is achieved to the E_{gap} calculation with the modified functional.

Table 1. Lattice parameters (a = b and c) (Å) and band gap energy (E_{gap}) (eV), and relative error concerning average experimental value in parenthesis.

Functional	a (Å)	c (Å)	E_{gap} (eV)
B1WC	5.62 (0.8 %)	12.53 (2.1 %)	5.28 (22.8 %)
B1WC (8%)	5.63 (1.0 %)	12.54 (2.1 %)	4.53 (3.6 %)
Reference Data	5.57[a], 5.58[b]	12.79[a], 12.82[b]	4.33[c], 4.25[d], and 4.54[e]

References: a [50], b [51], c [52], d [53], and e [51].

From the optimized crystalline structure were constructed symmetric and stoichiometric surface models corresponding to the crystallographic directions: (001), (100), (101), (103), (110), (111), (112) and (211). These surface models (2D) are finite in the *z*-direction but periodic in the plane.

It is important to emphasize that the successes of surface simulations depend on the model thickness (l) to ensure no interactions between the outermost layers and to guarantee surface energy (E_{surf}) convergence, which can be calculated through the formula $E_{surf} = (E_{slab} - nE_{bulk})/2\,A$, where E_{slab} is the total energy per unit cell of the slab in the $[hkl]$ direction, the E_{bulk} is the total energy of the BMO bulk per molecular unit, n is the number of bulk units, and A is the surface unit cell area [33,54].

The E_{surf} convergency was reached in 10, 16, 16, 8, 8, 16, 8 and 10 bulk units for (001), (100), (101), (103), (110), (111), (112), and (211) surfaces, respectively. As mentioned in the introduction section, connecting the surface energy calculation and the Wulff theory, it is possible to make a detailed road map of the NPs morphological transformations [35,55,56]. VESTA software [57] was employed to elaborate the morphological road map.

4. Results and discussion

4.1. Bulk

Figures 1a and 1b depict the representation of the BMO tetragonal unit cell (space group I41/a) with [BaO_8] and [MoO_4] clusters, which are the building blocks of the BMO. Figures 1c and 1d show the simulated XRD patterns and Raman spectra of the BMO with the calculated lattice parameters (*a* = *b* = 5.63 Å and *c* = 12.54 Å). From the simulated XRD data, we can see in Figure 1c peaks well-defined in 2ϴ = 26.5°, 27.8°, 32.1°, 42.9°, 45.9°, 48.4°, 53.8°, 54.5° and 68.9°, which correspond to diffractions from (112), (004), (200), (204), (220), (116), (312), (224) and (136) planes of tetragonal BMO structure. These theoretical results agree with experimental data [58–61].

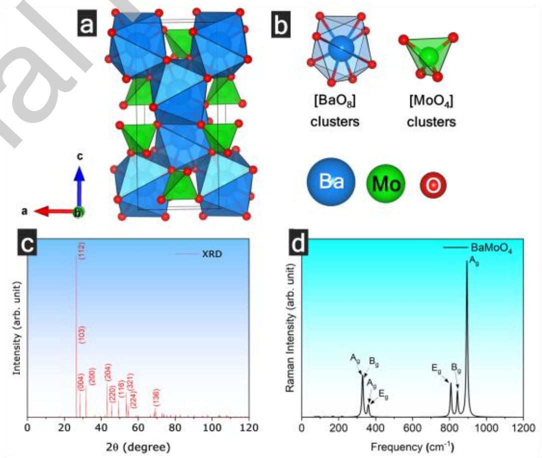

Figure 1. (a) BMO unit cell, (b) [BaO_8] and [MoO_4] clusters building blocks, (c) XRD pattern was determined through the RIETAN-RF [62] package implemented in the VESTA software [57] and (d) vibrational Raman spectrum.

The primitive cell of BMO has 36 zone-center phonon modes in the Raman spectrum: $\Gamma = 3A_g + 5A_u + 5B_g + 3B_u + 10E_g + 10E_u$, where the $3B_u$ are silent modes, $A_u + 2E_u$ acoustic modes. The $3A_g + 5B_g + 10E_g$ modes are active Raman-active optical modes and $4A_u + 8E_u$ IR-active modes (see Supplementary Material, Figure S1).

In the A_g modes, the Ba and Mo atoms remain immobile, and the motions are attributed to the O atoms. Thus, the A_g modes are usually symmetric to the rotation of the principal axis. On the other hand, the B_g modes are antisymmetric to the rotation of the principal axis, and the E_g modes are doubly degenerate, with inversion symmetry. Regarding the B_g, modes, it is verified that the main motion is associated with deformations of the $[MoO_4]^{2-}$ clusters. The Ba atoms move in the R_1 and R_6, while they remain static in the R_{11}, R_{12} e R_{17} modes. Some works [44,63–65] usually report the existence of only 13 active Raman modes for scheelite structures ($\Gamma = 3A_g + 5B_g + 5E_g$), this occurs because it is not considered that the E_g modes are doubly degenerate. For the R_2 e R_3 modes, the motion is associated with the $[BaO_8]$ cluster rotation. The $[MoO_4]$ cluster rotations with quasi-static Ba atoms characterize the R_4 and R_5 modes. In the R_{13} e R_{14} modes, oxygen atoms move with static Ba and Mo atoms. The R_{15} e R_{16} modes are characterized by the motion of only one O atom of the $[MoO_4]$ clusters.

The calculated Raman spectrum is represented in Figure 1c. The most intense peak corresponds to R_{18} (894 cm^{-1}) mode, which is preceded by two different bands associated with R_{17} (843 cm^{-1}) and R_{15} and R_{17} (807 cm^{-1}). Two bands can be noted at ~350 cm^{-1}, one first is associated with R_{10} (328 cm^{-1}) and R_{11} (331 cm^{-1}) modes, and the other is relative to R_{12} (358 cm^{-1}) and R_{13} and R_{14} (362 cm^{-1}).

Next, the band structure and DOS of the BMO structure are shown in Figures 2a and 2b. The calculations demonstrate a direct band gap transition, 4.54 eV, at the Γ point (see Figure 2b). Also, these theoretical results demonstrate a negligible variation in the estimated E_{gap}, when compared to the experimental value reported near room temperature [66–69], suggesting that the methodology used is suitable for describing the electronic properties of these studied systems. Based on the DOS, it is found that the valence band (VB) is mainly attributed to the O atom contribution. On the other hand, the conduction band (CB) is associated with a major O atom contribution, followed by the Mo and Ba atoms, and a bandwidth absence of states of ~1 eV in the CB. Hence, an additional d-d interaction in CB region can, in principle, promote a two-photon resonance on the BMO. For a detailed description of the electronic structure, the partial density of states (pDOS) is taken (see Supplementary Material, Figure S2). Concerning Ba and Mo atoms, the most significant contributions on VB are associated with degenerate p_x and p_y orbitals and for CB with degenerate d_2 and d_3 orbitals. Considering O atoms, the most relevant intensities in CB and VB are from the p_x and p_y. In addition, it is well known that the synthesis parameters may lead to the formation of complex defects on the BMO lattice (at short-, medium- and long-range), thus promoting the appearance of intermediary electronic levels in the forbidden region, as well as, decreasing the difference between the VB and CB [70].

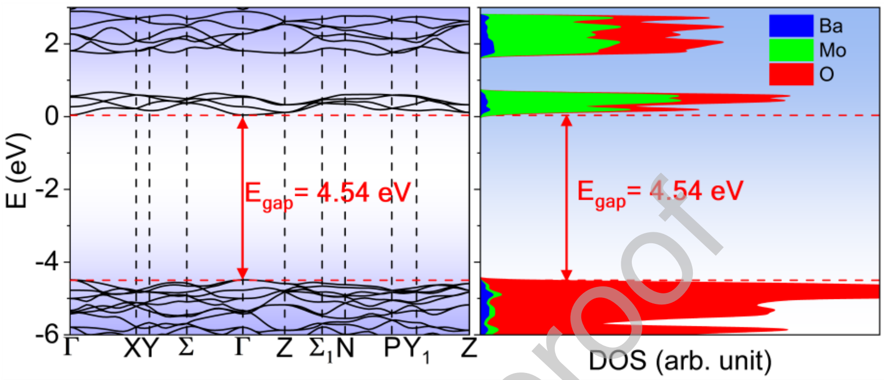

Figure 2. (a) Band structure and (b) Density of states of BMO bulk.

4.2. Surfaces properties

As is known, the surface is a region where the bulk structure is disrupted; therefore, the surface properties can significantly differ from the bulk, especially concerning atomic terminations [35,55,56]. These regions can be described in terms of their outermost clusters (Figure 3). Notice that the (001) and (112) surfaces are terminated on [BaO_6] and [MoO_4] clusters, while the (101), (100), (103), (100), (111) and (211) have [BaO_5] and [MoO_4] clusters.

To better understand the surface states, the Kroger-Vink notation [71] was employed to classify the outermost clusters. This notation describes a defect A with effective charge b occupying a lattice site a (A_a^b), and vacancies can be represented by V_a^b. Oxygen vacancies characterize the outermost clusters with coordination breakage and can be described as V_O^x, where the sub-index x indicates charge neutrality in the Kroger-Vink notation. Yet, the oxygen vacancies are usually responsible for the degree of structural order-disorder associated with distortions and changes in the bond lengths and angles between the outermost oxygen and barium atoms. Given this, the outermost undercoordinated clusters for (001) and (112) surfaces are [$BaO_6 . 2V_O^x$] and [$BaO_5 . 3V_O^x$] for (101), (100), (103), (100), (111) and (211).

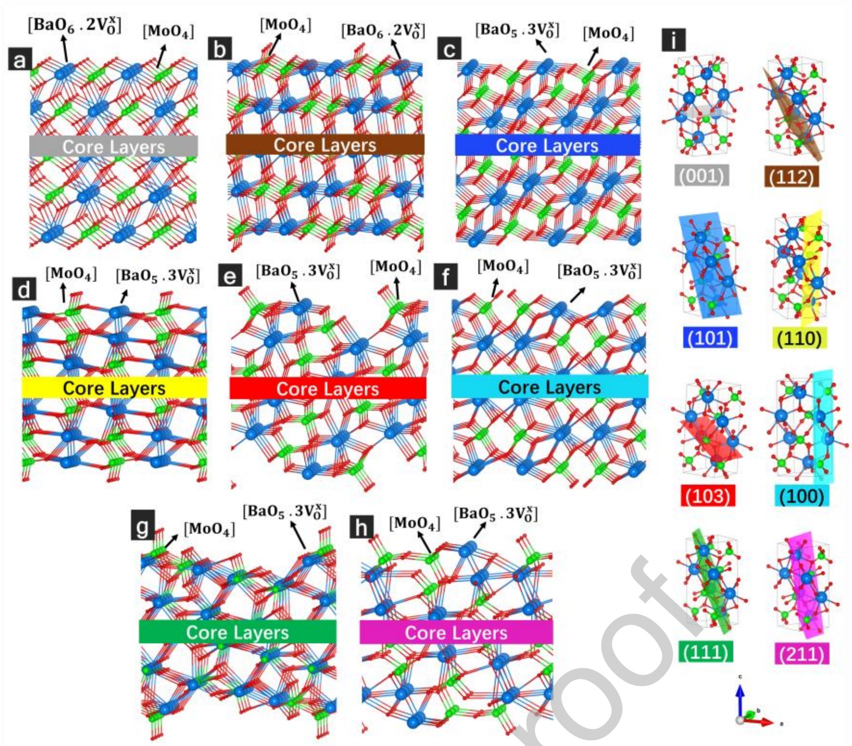

Figure 3. Outermost layers and $[BaO_6]$, $[BaO_5]$ and $[MoO_4]$ outermost clusters highlighted in the Kroger-Vink notation for (a) (001), (b) (112), (c) (101), (d) (110), (e) (103), (f) (100), (g) (111) and (h) (211) surfaces, and (i) cutting planes.

The number of nearby atoms on the BMO surface layers is the coordination number (CN). Notably, this property cannot describe the distortions during the crystal growth because the outermost layers have more freedom to relax, making them more prone to structural deformations based on the interaction with neighboring atoms, resulting in distorted outermost clusters. In contrast, the inner layers preserve the bulk structure, i.e., do not exhibit structural distortions. Therefore, the effective coordination number (ECoN) [72] can solve this problem, being an alternative to estimate cluster distortions. In this sense, the difference between CN and ECoN describes the relative cluster distortion.

Based on the E_{surf}, the stability order of the BMO surfaces is (001), (112), (101), (110), (103), (100), (111) and (211) (see Table 2). The outermost $[MoO_4]$ are significantly less distorted than $[BaO_x]$ clusters. This behavior suggests that in the BMO scheelite-type structures, the $[MoO_4]$ are rigid elements, and structural modifications can occur more easily in the $[BaO_x]$ clusters.

In addition, the decrease in surface stability with the *ECoN* (except by the (101) surface) is a trend that can be verified. The distinct behavior for (101) surface can be associated with the relative positions of outermost Ba and Mo: the only case where outermost Mo atoms occupy the innermost atomic layers compared to outermost Ba atoms.

Table 2. Surface energy (E_{surf}), band gap energy (E_{gap}), effective coordination number of outermost [BaO_x] ($ECoN_{[AO_x]}$) and [MoO_4] ($ECoN_{[BO_x]}$) cluster.

Surface	E_{surf} ($J.m^{-2}$)	E_{gap} (eV)	$ECoN_{[AO_x]}$	$ECoN_{[BO_x]}$
(001)	0.44	4.44	5.99	3.97
(112)	0.54	4.28	5.91	3.91
(101)	0.60	4.56	4.95	3.99
(110)	0.66	4.06	4.97	3.90
(103)	0.78	4.16	4.91	3.91
(100)	0.91	3.64	4.53	3.88
(111)	1.08	1.94	4.53	3.54
(211)	1.27	2.06	2.92	3.84

In the BMO surfaces, it is well known that the electronic properties depend on the cluster connectivity, $[O-Mo-O]$ and $[O-Ba-O]$ bond shifts, and the formation of oxygen vacancies due to a symmetry break between these clusters [46, 47]. The Figure 4a describes the DOS for the simulated surfaces, and it is verified that all surfaces have VB higher than the bulk, except the (101) surface. For all cases, the O states dominate the VB and CB. In the CB, the Mo contributions are similar to O, and Ba contributions are observed for the higher energies. The calculated band gap energy of surface states for (001), (112), (101), (110), (103), (100), (111), and (211) planes are 4.44, 4.28, 4.56, 4.06, 4.16, 3.64, 1.94, and 2.06 eV, respectively. Except for the (001), (101) and (112) surfaces, a lower DOS closer to the VB maximum is observed.

Figure 4b shows the top view of electrostatic potential isosurfaces, which can be used to evaluate the charge distribution on the outermost layers. The surfaces exhibit continuous bands of negative charge density intercalated by neutral regions where positive charge density accumulation can be found. Only the (100) surface does not obey this pattern, with continuous bands of positive charge density. These systems generally have a more pronounced nucleophilic character, except for the (101) surface.

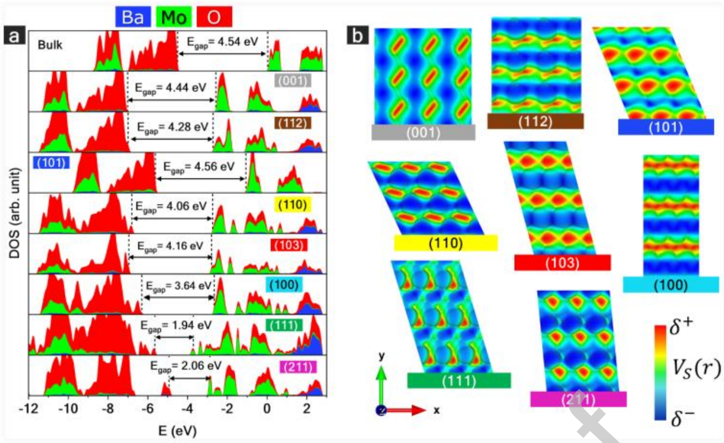

Figure 4. (a) Density of states of BMO surfaces following the relative stability order (from top to bottom) and (b) top view of the electrostatic potential surfaces ($V_S(r)$).

4.3. Transport Properties

When a semiconductor is irradiated with photons, in principle, the electrons (e^-) are excited and promoted to CB. In addition, holes (h^+) are left in the VB. After, e^- and h^+ are moved to the photocatalytic surface interface reactions according to the following equation: $semiconductor + hv \rightarrow e^- + h^+$. For the occurrence of this process, the photons must possess energy equal to or greater than the E_{gap} [73].

For semiconductors to be efficient photocatalysts, in addition to the electronic structure and optical property favorable to radiation absorption, electronic mobility is necessary for the fast transport velocity of electrons and reduce the probability of recombination of $e^- + h^+$ within the semiconductor and increase photocatalytic activity [74,75]. Hence, the mobility of photoexcited carriers can be evaluated indirectly by their effective carrier masses of electrons (m_e^*) and holes (m_h^*). To analyze the carrier stability, it can use the ratio m_{h^*}/m_{e^*}, for which desired values are lower than 0.5 or higher than 1.5 [76]. Here, the m_e^* and m_h^* were estimated by the parabolic fitting of the CB and VB by the following equation: $E = \hbar^2 k^2 / 2m^*$, with the distance between two consecutive k-points smaller than 0.002Å^{-1}, and then applying the reciprocal effective mass tensor, defined as:

$$\left(\frac{1}{m^*}\right)_{\mu\nu} = \frac{1}{\hbar}\frac{d^2 E_n(k)}{dk_\mu dk_\nu} \tag{1}$$

where $E_n(k)$ is the n-th band energy dispersion, k_μ and k_ν are the k-points in the BZ for the μ and ν directions, respectively. This approximation considers symmetric pathways, nevertheless the m_e^* and m_h^* can differ according to the high symmetry pathway considered.

To compare these values for each (*hkl*) direction was used the general effective mass of the hole or electron (m^*), which is calculated by the following expression:

$$\frac{n}{m^*} = \frac{1}{m_1^*} + \frac{1}{m_2^*} + \cdots + \frac{1}{m_{n-1}^*} + \frac{1}{m_n^*} \quad (2)$$

where n represents the number of high symmetry pathways of the band structure, m^* the general effective mass of hole or electron, m_n^* are the effective masses per pathway [77].

DOS analysis estimated the charge carrier concentration through Fermi-Dirac distribution, see equations (3) and (4), which relate to the Boltzmann constant (k_b), temperature (T), electronic DOS per unit cell volume ($D(\varepsilon)$), Fermi energy (ε_F), valence bands maximum (ε_{VB}) and conduction bands minimum (ε_{CB}). From the ρ_e and ρ_h values, the semiconductor nature can be determined. In n-type semiconductors, electrons are predominant charge carriers associated with higher states in CB. On the other hand, a higher number of states in VB region indicates a p-type semiconductor behavior, suggesting a greater presence of photogenerated electrons in CB.

$$\rho_e(T) = \int_{-\infty}^{\varepsilon_{CB}} D(\varepsilon) \left(\frac{1}{e^{((\varepsilon_F - \mu)/k_b T)} + 1}\right) d\varepsilon \quad (3)$$

$$\rho_h(T) = \int_{\varepsilon_{VB}}^{+\infty} D(\varepsilon) \left(\frac{1}{e^{((\mu - \varepsilon_F)/k_b T)} + 1}\right) d\varepsilon \quad (4)$$

It has been suggested by Bahers et al. [78] that to achieve good carrier mobility of the effective mass must be $m_e^* < 0.5$. However, most complex metal oxides have much higher effective mass values, usually in the range of 1 to 10 m_e^*, limiting carrier mobility [79]. Table 3 shows the effective mass of the electron (m_e^*/m_0) and hole (m_h^*/m_0), as well as the ratio (m_h^*/m_e^*). The bulk and the (001), (100) and (111) surfaces exhibit the m_e^*/m_0 values greater than the m_h^*/m_0. On the contrary, the (112), (101), (110), (103), and (211) surfaces have m_e^*/m_0 greater than the m_h^*/m_0. None of the evaluated surfaces have greater carrier mobility than the bulk. Except for (001) and (100) surfaces, all have m_h^*/m_e^* ratio suitable to photocatalytic processes.

Determining the m_e^* and m_h^* in these systems requires careful consideration, and alternative approaches, particularly a parabolic band fitting approach, were employed to determine the effective mass, resulting in unusually high values of effective mass for flat bands for some surfaces. These values follow the band structures shown in Figure S3 (see Supplementary Material), where it is possible to observe that surfaces with flattened bands around the band gap region, such as (111), exhibit quasi-planar bands.

The charge carrier density values (ρ_e and ρ_h) shows that BMO is an n-type semiconductor, as reported in the literature [80]. On the other hand, the surfaces are predominately n-type, except for (112) and (103), which are p-type. In addition, the (110) and (103) exhibit the highest ρ_e and ρ_h values, respectively. It is noted that the increase in the carrier density on the surface when compared to the bulk, may be associated with the high electropositive character of Ba^{2+}, which results in the lower diffusion of interstitial O^{2-} a known fact because of decreasing electrical conductivity [81]. In this regard, morphology control can promote mass transfer and quicken the charge flow, inducting the electron-hole separation at the material interface.

Table 3. Effective electron (m_e^*/m_0) and hole (m_h^*/m_0), ratio m_h^*/m_e^* and electrons (ρ_e) and holes (ρ_h) carrier density (10^{20} cm^{-3}) in 300 K.

	m_e^*/m_0	m_h^*/m_0	m_h^*/m_e^*	ρ_e	ρ_h	Type
bulk	5.39	2.20	0.41	0.42	0.34	n
(001)	5.65	5.27	0.93	17.51	8.87	n
(112)	7.59	26.49	3.49	7.06	32.06	p
(101)	7.49	18.44	2.46	37.62	13.74	n
(110)	5.67	13.02	2.30	365.81	69.72	n
(103)	6.75	23.61	3.50	1.99	228.28	p
(100)	17.70	16.91	0.96	30.63	23.66	n
(111)	1099.16	44.69	0.04	59.39	35.47	n
(211)	51.89	93.62	1.80	69.02	50.73	n

4.4. Morphological nanoparticles route

The complete BMO morphologies route is represented in Figure 5a, taking as a starting point the morphology obtained via Wulff theory and the present surface energies calculations (v_9). Certain degrees of structural organization can also be achieved when the material is subjected to certain experimental conditions to obtain different morphologies, some of which are described in the morphological mapping (see Figure 5).

According to Figure 5b, the decrease of $E_{surf}^{(001)}$ results in disk-like morphologies, $E_{surf}^{(112)}$, $E_{surf}^{(101)}$, $E_{surf}^{(111)}$, $E_{surf}^{(103)}$ or $E_{surf}^{(221)}$ minimizations favor the formation of octahedral morphologies, and those associated with (112) and (103) are more flattening than the others. Finally, $E_{surf}^{(110)}$ or $E_{surf}^{(100)}$ decreases result in rod-like morphologies. Understanding the exposed surfaces in a giver morphology is essential for experimentalists. From this perspective, it is well known that a predominance of highly reactive facets in BMO nano/microstructures may enhance their photocatalytic performance in many reactions of interest [82–84].

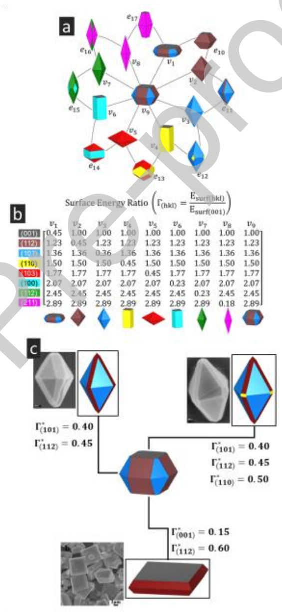

Figure 5. (a) BMO morphologies with all possible variations for surfaces with maximum exposed areas and combined two by two, according to the methodology reported by Laranjeira et al. [56], (b) Surface energy ratio matrix, and (c) morphological modulations proposed given from the morphology estimated via DFT calculations to obtain experimental morphologies [85,86]. Reprinted (adapted) with permission from *Cryst. Growth Des.* 2008, 8, 7, 2275–2281. Copyright 2023 American Chemical Society.

Another factor that should be considered is that the BMO exhibits photoluminescent (PL) properties; however, the origin and mechanisms of PL emissions in metallic molybdates are not yet fully understood. According to Marques et al. [87], intermediate energy levels within the band gap are caused by distortions of the [MoO_4] clusters, which are mainly composed of O 2p orbitals (above the VB) and Mo 4d orbitals (below the CB). Wu et al. [88] indicated that slightly distorted tetrahedral symmetry leads to a structured absorption band for the $A_1 \rightarrow T_{2(1)}$ transition, which induces blue PL emission in BMO microcrystals.

The surface energy ratio matrix finds application in estimating the DOS of nano/microstructures. Previous works have reported a simple additive linear model that directly analyzes the electronic contributions of each exposed facet of a given material [55,56]. Hence, from this perspective, materials with a single exposed surface are expected to exhibit a DOS equivalent to the exposed facet. For those with two or more exposed surfaces display a combination of electronic contributions from these facets. For instance, the balanced DOS of the ideal morphology (Figure 6a) was developed using this model. Notably, the energy gap of surface states is determined by the surfaces with the highest VB and the lowest CB, which are the (101) and (112) surfaces, respectively. As a result, nano/microstructures with the same exposed surfaces as the ideal morphology (v_9) are expected to have an energy gap of surface states of about 2.91 eV. Other authors have observed that the profile PL emission for various wide band gap semiconductors is mainly due to surface state defect levels [9–12,89–92]. In this sense, Wang et al. [13] reported BMO nanoparticles with rhombohedral morphology and achieved a maximum PL emission band at ~2.8 eV, a value closer than the v_9 estimated energy gap of surface states.

Figure 6b illustrates the band gap energy of surface states for various morphologies presented in the general map above (see Figure 5). While v_1 and v_9 exhibit identical in terms of the energy band gap of surface states, the relative contribution of each facet varies. Notably, the estimated energy gap of surface states may range from 1.21 eV (v_8) to 4.56 eV (v_3), indicating that morphology is decisive in determining the surface states of BMO NPs. Generally, BMO NPs with the (101), (111), and (211) exposed facets tend to exhibit lower band gap energy than others. Sun [93] synthesized BMO with different morphologies (shuttle-like and flower-shaped) induced by ethanol and observed enhanced PL response. In particular, the shuttle-like morphology has a similar aspect to v_8 morphology, which has a band gap energy of 2.06 eV and exhibits PL emission for 500-550 nm, which corresponds to 2.48-2.26 eV, closer than the v_8.

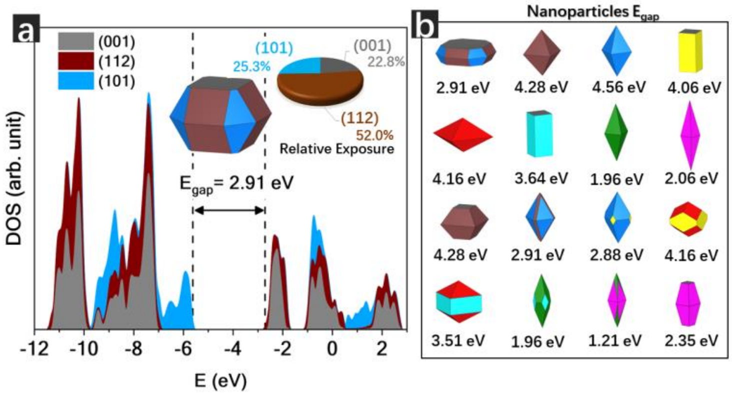

Figure 6. (a) Density of states for each surface exposed on the ideal morphology balanced by its relative exposure ratio, and (b) an estimative of the band gap energy of the nanoparticles present in the morphological mapping using the balanced DOS.

4.5. Photocatalytic activity

Recently, several researchers reported different morphologies of scheelite compounds with photocatalytic activity for organic pollutants removal from wastewater [94,95]. Reactive oxygen species ($\bullet OH$, $O_2^{\bullet-}$ and $\bullet OOH$) can interact with organic pollutants in water resulting in various intermediaries depending on the pollutant.

The $O_2^{\bullet-}$ radical is generated when O_2 react with the photoexcited electron in CB (Eq. 5). The $O_2^{\bullet-}$ can be protonated to form the hydroperoxyl ($\bullet OOH$) (Eq. 6) and the hydrogen peroxide (H_2O_2) (Eq. 7).

$$e^- + O_2 \rightarrow O_2^{\bullet-} \quad (5)$$

$$O_2^{\bullet-} + H^+ \rightarrow HOO^\bullet \quad (6)$$

$$2HOO^\bullet \rightarrow O_2 + H_2O_2 \quad (7)$$

The radical hydroxyl production can occur through two routes: (i) in an aqueous environment H_2O and OH^- are oxidized by h^+ photogenerated to produce the radical $HO^\bullet$ (Eq. 8) or (ii) the H_2O_2 formed in Eq. 7 can be decomposed to produce the $HO^\bullet$ (Eq. 9).

$$h^+ + H_2O \rightarrow HO^\bullet + H^+ \quad (8)$$

$$h^+ + HO^- \rightarrow HO^\bullet \quad (9)$$

It is reported that some scheelite ABO_4 structures possess the capacity for photochemical hydrogen production [82]. Eq. 10 shows the total reaction for this process and can be obtained from the two elemental reactions (Eq. 11 and 12). To occur this phenomenon, it is necessary E_{gap} values higher than 1.23 eV (visible light covering range). In this regard, BMO surfaces have an adequate E_{gap} for this process. In addition, the occurrence of the mechanism also depends on the appropriate band edge positions (band alignment). The CBM should be above of reduction potential H^+/H_2 and the VBM below of oxidation potential O_2/H_2O.

$$H_2O \rightarrow H_2 + 1/2\,O_2 \quad (10)$$

$$2H_2O \rightarrow O_2 + 4H^+ + 4e^- \quad (11)$$

$$2H_2O + 2e^- \rightarrow H_2 + 2HO^- \quad (12)$$

According to band alignment (Figure 7), the (101) surface is the only one with the band edge positions favorable to the occurrence of all processes mentioned. All surfaces can reduce the O_2 to $^{\bullet}O_2^-$ and the H^+ to H_2. Except for the (111), all surfaces can oxide the O_2 to H_2O and $^{\bullet}O_2^-$ to H_2O_2. The (101) surface is unique that can oxide the OH^- to $^{\bullet}OH$, this way, dye photodegradation mechanisms via hydroxyl radicals can occur in the BMO-based system where the (101) is exposed. The bulk structure is promising in oxidative processes, with band edge positions favorable for the $OH^-/$ $^{\bullet}OH$, H_2O/O_2 and $^{\bullet}O_2^-/H_2O_2$ reactions, on the other hand, the reduction process H^+/H_2 and $O_2/$ $^{\bullet}O_2^-$ not occur due to the lower position of the CBM.

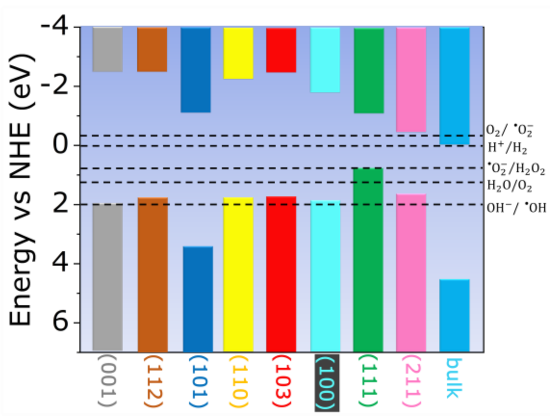

Figure 7. Band edge alignment for BMO surfaces, based on the methodology reported by Toroker et al. [96]. The positions of the conduction band minimum (E_{CBM}) and the

valence band maximum (E_{VBM}) are defined by $E_{CBM/VBM} = E_{BGC} \pm 0.5E_{gap} - E_e$, where E_{BGC} is the energy of the band gap center, and E_e is the Normal Hydrogen Electrode (NHE) potential (4.44 eV).

Yanalak et al. [97] investigated the photocatalytic hydrogen evolution using BMO and $BaWO_4$ as catalysts with triethanolamine and eosin-Y as a sacrificial agent and visible-light-sensitizer, respectively. The results demonstrate that the BMO and $BaWO_4$ are capable of hydrogen production. For BMO, these results agree with the band alignment predicted herein.

Bazarganipour [23] has been synthesized rod-like and sphere-like BMO nanostructures by a large-scale and simple sonochemical method using as precursors $Ba(Sal)_2$ (Sal = salicylidene) and $Na_2MoO_4.2H_2O$. The shape was controlled by varying the surfactant and power source, and it was verified that the BMO nanostructures could remove the methylene blue dye. It is pointed out that the $^{\bullet}OH$ as mainly responsible for methylene blue degradation. However, for rod-like, this is in disagreement with results for the (100) and (110) surfaces (associated with rod-like morphologies, the v_4 and v_6 in Figure 5) do not have band alignment adequately for $^{\bullet}OH$ production. For rod-like morphologies, dye degradation can occur only by h^+ or $^{\bullet}O_2^-$ radicals.

5. Conclusions

This paper reports the BMO surface-dependent properties via DFT simulations and their influence on BMO nanoparticles. According to the results, the surface stability order is (001) > (112) > (101) > (110) > (103) > (100) > (111) > (211). For (001), (112), (101), (110), (103), (100), (111), and (211) are observed E_{gap} values of 4.44, 4.28, 4.56, 4.06, 4.16, 3.64, 1.94, and 2.06 eV, respectively. The BMO surfaces are predominately n-type, except for (112) and (103). Also, the electronic and structural surface properties depend strongly on the polyhedron connectivity, $[O - Mo - O]$ and $[O - Ba - O]$ bond shifts, and the formation of oxygen vacancies due to a symmetry break between the bonded clusters.

The band alignment reveals that all surfaces can be used to reduce the O_2 to $^{\bullet}O_2^-$ and the H^+ to H_2, and except for the (111), all surfaces can oxide the O_2 to H_2O and $^{\bullet}O_2^-$ to H_2O_2. The (101) surface is unique that can oxide the OH^- to $^{\bullet}OH$, this way, a condition necessary to dye photodegradation mechanisms via hydroxyl radicals is that the (101) are exposed.

By the Wulff construction, a detailed mapping of NPs morphological transformation routes was possible. Notably, this finding demonstrates that the predicted morphologies by design rules may help elucidate surface states of BMO nano/microstructures that are critical in their photophysical properties. Therefore, our results are expected to be useful for analyzing and predicting the experimental results of the $BaMoO_4$ and related systems. The (001) surface exhibits disk-like morphology, (112), (101), (103), (111) and (211) possess octahedral morphologies, and the (110) and (100) rod-like morphologies.

6. References

[1] B.G. Alamani, J.D. Gale, J.D. Rimer, Zinc Ions Modify Calcium Oxalate Growth by Distinct Transformation of Crystal Surface Termination, Cryst Growth Des. 21 (2021) 3375–3383. https://doi.org/10.1021/ACS.CGD.1C00166/SUPPL_FILE/CG1C00166_SI_004.MP4.

[2] L.H. da S. Lacerda, M.A. San-Miguel, S.R. de Lazaro, Surface and morphological studies of LiNbO 3 : p-type semiconductivity on stoichiometric surfaces, New Journal of Chemistry. 45 (2021) 16594–16605. https://doi.org/10.1039/D1NJ02429A.

[3] L.H. da S. Lacerda, M.A. San-Miguel, DFT approaches unraveling the surface and morphological properties of MnMoO4, Appl Surf Sci. 567 (2021) 150882. https://doi.org/10.1016/J.APSUSC.2021.150882.

[4] Z. Yan, W. Xue, D. Mei, Density Functional Theory Study on the Morphology Evolution of Hydroxylated β-Cristobalite Silica and Desilication in the Presence of Methanol, Journal of Physical Chemistry C. 125 (2021) 7868–7879. https://doi.org/10.1021/ACS.JPCC.0C11368/SUPPL_FILE/JP0C11368_SI_001.PDF.

[5] Y. Li, Q. Liu, W. Shen, Morphology-dependent nanocatalysis: metal particles, Dalton Transactions. 40 (2011) 5811–5826. https://doi.org/10.1039/C0DT01404D.

[6] A.F. Gouveia, L. Gracia, E. Longo, M.A. San-Miguel, J. Andrés, Modulating the properties of multifunctional semiconductors by means of morphology: Theory meets experiments, Comput Mater Sci. 188 (2021) 110217. https://doi.org/10.1016/J.COMMATSCI.2020.110217.

[7] J. Andrés, L. Gracia, A.F. Gouveia, M.M. Ferrer, E. Longo, Effects of surface stability on the morphological transformation of metals and metal oxides as investigated by first-principles calculations, Nanotechnology. 26 (2015) 405703. https://doi.org/10.1088/0957-4484/26/40/405703.

[8] M. Ghiyasiyan-Arani, M. Salavati-Niasari, A.F. Zonouz, Effect of Operational Synthesis Parameters on the Morphology and the Electrochemical Properties of 3D Hierarchical AlV3O9 Architectures for Li-Ion Batteries, J Electrochem Soc. 167 (2020) 020544. https://doi.org/10.1149/1945-7111/AB6C5A.

[9] J.P.A. de Jesus, A.C.L. Santos, F.M. Pinto, C.A. Taft, F.A. La Porta, Review: theoretical and experimental investigation of the intrinsic properties of Zn2GeO4 nanocrystals, Journal of Materials Science 2020 56:7. 56 (2020) 4552–4568. https://doi.org/10.1007/S10853-020-05549-8.

[10] V.Y. Suzuki, L.H.C. Amorin, G.S.L. Fabris, S. Dey, J.R. Sambrano, H. Cohen, D. Oron, F.A. La Porta, Enhanced Photocatalytic and Photoluminescence Properties Resulting from Type-I Band Alignment in the Zn2GeO4/g-C3N4 Nanocomposites, Catalysts 2022, Vol. 12, Page 692. 12 (2022) 692. https://doi.org/10.3390/CATAL12070692.

[11] V.Y. Suzuki, L.H.C. Amorin, N.M. Lima, E.G. Machado, P.E. Carvalho, S.B.R. Castro, C.C.S. Alves, A.P. Carli, M.S. Li, E. Longo, F.A. La Porta, Characterization of the structural, optical, photocatalytic and in vitro and in vivo anti-inflammatory properties of Mn2+ doped Zn2GeO4 nanorods, J Mater Chem C Mater. 7 (2019) 8216–8225. https://doi.org/10.1039/C9TC01189G.

[12] V.Y. Suzuki, N.H. de Paula, R. Gonçalves, M.S. Li, E.C. Pereira, E. Longo, F.A. La Porta, Exploring effects of microwave-assisted thermal annealing on optical properties of Zn2GeO4 nanostructured films, Materials Science and Engineering: B. 246 (2019) 7–12. https://doi.org/10.1016/J.MSEB.2019.05.023.

[13] Y. Wang, H. Gao, S. Wang, L. Fang, X. Chen, C. Yu, S. Tang, H. Liu, Z. Yi, H. Yang, Facile synthesis of BaMoO4 and BaMoO4/BaWO4 heterostructures with type -I band arrangement and enhanced photoluminescence properties, Advanced Powder Technology. 32 (2021) 4186–4197. https://doi.org/10.1016/J.APT.2021.09.028.

[14] G. Yanalak, A. Ozen, A. Sarılmaz, A. Keles, E. Aslan, F. Ozel, I. Hatay Patir, Scheelite-type BaMoO4 and BaWO4 based dye sensitized photocatalytic hydrogen evolution by water splitting, Journal of Physics and Chemistry of Solids. 168 (2022) 110821. https://doi.org/10.1016/J.JPCS.2022.110821.

[15] S. Vidya, A. John, S. Solomon, J.K. Thomas, Optical and dielectric properties of $SrMoO_4$ powders prepared by the combustion synthesis method, Advances in Materials Research. 1 (2012) 191–204. https://doi.org/10.12989/AMR.2012.1.3.191.

[16] A.M. Huerta-Flores, I. Juárez-Ramírez, L.M. Torres-Martínez, J.E. Carrera-Crespo, T. Gómez-Bustamante, O. Sarabia-Ramos, Synthesis of AMoO4 (A = Ca, Sr, Ba) photocatalysts and their potential application for hydrogen evolution and the degradation of tetracycline in water, J Photochem Photobiol A Chem. 356 (2018) 29–37. https://doi.org/10.1016/J.JPHOTOCHEM.2017.12.029.

[17] C. Cui, J. Bi, C. Wu, S. Zhang, D. Gao, Novel electrochemical technique: Grain control in preparation of polycrystalline BaMoO4 film, Mater Res Bull. 43 (2008) 1160–1163. https://doi.org/10.1016/J.MATERRESBULL.2007.06.001.

[18] A.P.A. Marques, F.C. Picon, D.M.A. Melo, P.S. Pizani, E.R. Leite, J.A. Varela, E. Longo, Effect of the order and disorder of BaMoO 4 powders in photoluminescent properties, J Fluoresc. 18 (2008) 51–59. https://doi.org/10.1007/S10895-007-0237-6/TABLES/4.

[19] Y. Mi, Z. Huang, F. Hu, X. Li, Room temperature reverse-microemulsion synthesis and photoluminescence properties of uniform BaMoO4 submicro-octahedra, Mater Lett. 63 (2009) 742–744. https://doi.org/10.1016/J.MATLET.2008.12.047.

[20] C. Zhang, E. Shen, E. Wang, Z. Kang, L. Gao, C. Hu, L. Xu, One-step solvothermal synthesis of high ordered BaWO4 and BaMoO4 nanostructures, Mater Chem Phys. 96 (2006) 240–243. https://doi.org/10.1016/J.MATCHEMPHYS.2005.06.061.

[21] L.D.S. Alencar, A. Mesquita, C.A.C. Feitosa, R. Balzer, L.F.D. Probst, D.C. Batalha, M.G. Rosmaninho, H. V. Fajardo, M.I.B. Bernardi, Preparation, characterization and catalytic application of Barium molybdate (BaMoO4) and Barium tungstate (BaWO4) in the gas-phase oxidation of toluene, Ceram Int. 43 (2017) 4462–4469. https://doi.org/10.1016/J.CERAMINT.2016.12.096.

[22] M. Ghaed-Amini, M. Bazarganipour, M. Salavati-Niasari, K. Saberyan, Morphology and photoluminescence of BaMoO4 micro- and nano-crystals synthesized by coprecipitation method, Transactions of Nonferrous Metals Society of China. 25 (2015) 3967–3973. https://doi.org/10.1016/S1003-6326(15)64045-6.

[23] M. Bazarganipour, Synthesis and characterization of BaMoO4 nanostructures prepared via a simple sonochemical method and their degradation ability of methylene blue, Ceram Int. 42 (2016) 12617–12622. https://doi.org/10.1016/J.CERAMINT.2016.04.151.

[24] Y.Q. Mao, J.G. Wei, Y. Zou, L.P. Zhu, Controllable synthesis, characterization and photoluminescence properties of flower-like BaMoO4 hierarchical architectures, CrystEngComm. 22 (2020) 3115–3121. https://doi.org/10.1039/D0CE00371A.

[25] A.M. Huerta-Flores, I. Juárez-Ramírez, L.M. Torres-Martínez, J.E. Carrera-Crespo, T. Gómez-Bustamante, O. Sarabia-Ramos, Synthesis of AMoO4 (A = Ca, Sr, Ba) photocatalysts and their potential application for hydrogen evolution and the degradation of tetracycline in water, J Photochem Photobiol A Chem. 356 (2018) 29–37. https://doi.org/10.1016/J.JPHOTOCHEM.2017.12.029.

[26] L.S. Cavalcante, J.C. Sczancoski, R.L. Tranquilin, J.A. Varela, E. Longo, M.O. Orlandi, Growth mechanism of octahedron-like BaMoO4 microcrystals processed in microwave-hydrothermal: Experimental observations and computational modeling, Particuology. 7 (2009) 353–362. https://doi.org/10.1016/J.PARTIC.2009.05.002.

[27] M.C. Oliveira, L. Gracia, I.C. Nogueira, M.F.C. Gurgel, J.M.R. Mercury, E. Longo, J. Andrés, On the morphology of BaMoO4 crystals: A theoretical and experimental approach, Crystal Research and Technology. 51 (2016) 634–644. https://doi.org/10.1002/CRAT.201600227.

[28] M. Ghaed-Amini, M. Bazarganipour, M. Salavati-Niasari, K. Saberyan, Morphology and photoluminescence of BaMoO4 micro- and nano-crystals synthesized by coprecipitation method, Transactions of Nonferrous Metals Society of China. 25 (2015) 3967–3973. https://doi.org/10.1016/S1003-6326(15)64045-6.

[29] F.A. La Porta, C.A. Taft, eds., Functional Properties of Advanced Engineering Materials and Biomolecules, (2021). https://doi.org/10.1007/978-3-030-62226-8.

[30] F. de A. La Porta, C.A. Taft, eds., Emerging Research in Science and Engineering Based on Advanced Experimental and Computational Strategies, (2020). https://doi.org/10.1007/978-3-030-31403-3.

[31] E. Longo, F. de Almeida La Porta, Recent advances in complex functional materials: From design to application, Recent Advances in Complex Functional Materials: From

Design to Application. (2017) 1–454. https://doi.org/10.1007/978-3-319-53898-3/COVER.

[32] G. Wulff, XXV. Zur Frage der Geschwindigkeit des Wachsthums und der Auflösung der Krystallflächen, Z Kristallogr Cryst Mater. 34 (1901). https://doi.org/10.1524/zkri.1901.34.1.449.

[33] A.R. Albuquerque, I.M.G. Santos, J.R. Sambrano, Propriedades estruturais e eletrônicas de nanofilmes de TiO2 anatase: cálculos B3LYP-D* em sistemas periódicos bidimensionais, Quim Nova. 37 (2014) 1318–1323. https://doi.org/10.5935/0100-4042.20140187.

[34] M.M. Ferrer, G.S.L. Fabris, B. V. de Faria, J.B.L. Martins, M.L. Moreira, J.R. Sambrano, Quantitative evaluation of the surface stability and morphological changes of Cu2O particles, Heliyon. 5 (2019). https://doi.org/10.1016/j.heliyon.2019.e02500.

[35] J.A.S. Laranjeira, S.A. Azevedo, G.S.L. Fabris, A.R. Albuquerque, M.M. Ferrer, J.R. Sambrano, Surface-dependent properties and morphological transformations of rutile GeO2 nanoparticles, Appl Surf Sci. 609 (2023) 155321. https://doi.org/10.1016/J.APSUSC.2022.155321.

[36] T. Yan, B. Sun, A.S. Barnard, Predicting archetypal nanoparticle shapes using a combination of thermodynamic theory and machine learning, Nanoscale. 10 (2018) 21818–21826. https://doi.org/10.1039/C8NR07341D.

[37] M. Huang, C. Sun, X. Zhang, P. Wang, S. Xu, X.R. Shi, The surface structure, stability, and catalytic performances toward O2 reduction of CoP and FeCoP2, Dalton Transactions. 51 (2022) 10420–10431. https://doi.org/10.1039/D2DT01408D.

[38] H. Zhao, F. Zhang, X. Guo, Q. Zhang, T. Liu, Ab initio study of electronic structures of BaMoO4 crystals containing an interstitial oxygen atom, Journal of Physics and Chemistry of Solids. 71 (2010) 1639–1643. https://doi.org/10.1016/J.JPCS.2010.08.013.

[39] W. Kohn, L.J. Sham, Self-consistent equations including exchange and correlation effects, Physical Review. 140 (1965) A1133. https://doi.org/10.1103/PHYSREV.140.A1133/FIGURE/1/THUMB.

[40] T. Qin, Q. Wang, L. Wang, H. Yan, C. Liu, Y. Han, Y. Ma, C. Gao, High-pressure dielectric behavior of BaMoO4: a combined experimental and theoretical study, Physical Chemistry Chemical Physics. 18 (2016) 33109–33114. https://doi.org/10.1039/C6CP06323C.

[41] H. Pecinatto, C. Mota, H.O. Frota, Determination of the mechanical, thermal, electronic and optoelectronics properties of BaMoO4 with oxygen vacancy by ab-initio calculations, Mater Today Commun. 34 (2023). https://doi.org/10.1016/j.mtcomm.2022.105074.

[42] R. Dovesi, R. Orlando, B. Civalleri, C. Roetti, V.R. Saunders, C.M. Zicovich-Wilson, CRYSTAL: A computational tool for the ab initio study of the electronic properties of crystals, Zeitschrift Fur Kristallographie. 220 (2005) 571–573. https://doi.org/10.1524/ZKRI.220.5.571.65065/MACHINEREADABLECITATION/RIS.

[43] D.I. Bilc, R. Orlando, R. Shaltaf, G.M. Rignanese, J. Íñiguez, P. Ghosez, Hybrid exchange-correlation functional for accurate prediction of the electronic and structural properties of ferroelectric oxides, Phys Rev B Condens Matter Mater Phys. 77 (2008) 165107. https://doi.org/10.1103/PHYSREVB.77.165107/FIGURES/4/MEDIUM.

[44] E.O. Gomes, G.S.L. Fabris, M.M. Ferrer, F. V. Motta, M.R.D. Bomio, J. Andres, E. Longo, J.R. Sambrano, Computational procedure to an accurate DFT simulation to solid state systems, Comput Mater Sci. 170 (2019) 109176. https://doi.org/10.1016/j.commatsci.2019.109176.

[45] S. Piskunov, E. Heifets, R.I. Eglitis, G. Borstel, Bulk properties and electronic structure of SrTiO3, BaTiO3, PbTiO3 perovskites: an ab initio HF/DFT study, Comput Mater Sci. 29 (2004) 165–178. https://doi.org/10.1016/J.COMMATSCI.2003.08.036.

[46] F. Corà, A. Patel, N.M. Harrison, R. Dovesi, C.R.A. Callow, An ab Initio Hartree−Fock Study of the Cubic and Tetragonal Phases of Bulk Tungsten Trioxide, J Am Chem Soc. 118 (1996) 12174–12182. https://doi.org/10.1021/JA961514U.

[47] T. Bredow, K. Jug, R.A. Evarestov, Electronic and magnetic structure of ScMnO3, Physica Status Solidi (b). 243 (2006) R10–R12. https://doi.org/10.1002/PSSB.200541403.

[48] M. Ferrero, M. Ŕrat, R. Orlando, R. Dovesi, Coupled perturbed Hartree-Fock for periodic systems: The role of symmetry and related computational aspects, J Chem Phys. 128 (2008) 014110. https://doi.org/10.1063/1.2817596.

[49] M. Perrero, M. Rérat, R. Orlando, R. Dovesi, The calculation of static polarizabilities of 1-3D periodic compounds. the implementation in the crystal code, J Comput Chem. 29 (2008) 1450–1459. https://doi.org/10.1002/JCC.20905.

[50] J.C. Sczancoski, L.S. Cavalcante, N.L. Marana, R.O. da Silva, R.L. Tranquilin, M.R. Joya, P.S. Pizani, J.A. Varela, J.R. Sambrano, M. Siu Li, E. Longo, J. Andrés, Electronic structure and optical properties of BaMoO4 powders, Current Applied Physics. 10 (2010) 614–624. https://doi.org/10.1016/j.cap.2009.08.006.

[51] A.A.G. Santiago, C.R.R. Almeida, R.L. Tranquilin, R.M. Nascimento, C.A. Paskocimas, E. Longo, F. V. Motta, M.R.D. Bomio, Photoluminescent properties of the Ba1−xZnxMoO4 heterostructure obtained by ultrasonic spray pyrolysis, Ceram Int. 44 (2018) 3775–3786. https://doi.org/10.1016/J.CERAMINT.2017.11.161.

[52] L.D.S. Alencar, A. Mesquita, C.A.C. Feitosa, R. Balzer, L.F.D. Probst, D.C. Batalha, M.G. Rosmaninho, H. V. Fajardo, M.I.B. Bernardi, Preparation, characterization and catalytic application of Barium molybdate (BaMoO4) and Barium tungstate (BaWO4) in the gas-phase oxidation of toluene, Ceram Int. 43 (2017) 4462–4469. https://doi.org/10.1016/j.ceramint.2016.12.096.

[53] M. Bazarganipour, Synthesis and characterization of BaMoO4 nanostructures prepared via a simple sonochemical method and their degradation ability of methylene blue, Ceram Int. 42 (2016) 12617–12622. https://doi.org/10.1016/j.ceramint.2016.04.151.

[54] A.F. Gouveia, M.M. Ferrer, J.R. Sambrano, J. Andrés, E. Longo, Modeling the atomic-scale structure, stability, and morphological transformations in the tetragonal phase of LaVO4, Chem Phys Lett. 660 (2016) 87–92. https://doi.org/10.1016/j.cplett.2016.08.013.

[55] J.A.S. Laranjeira, G.S.L. Fabris, A.R. Albuquerque, M.M. Ferrer, J.R. Sambrano, Morphological transformations mapping of CaXO4 (X = Mo or W) and their surface stability, Mater Today Commun. (2022) 104178. https://doi.org/10.1016/J.MTCOMM.2022.104178.

[56] J.A.S. Laranjeira, G.S.L. Fabris, M.M. Ferrer, A.R. Albuquerque, J.R. Sambrano, Morphological Transformation Network of Nanoparticles via DFT Simulations, Cryst Growth Des. 20 (2020) 4600–4611. https://doi.org/10.1021/acs.cgd.0c00423.

[57] K. Momma, F. Izumi, VESTA: a three-dimensional visualization system for electronic and structural analysis, Urn:Issn:0021-8898. 41 (2008) 653–658. https://doi.org/10.1107/S0021889808012016.

[58] H. Pecinatto, C. Mota, H.O. Frota, Determination of the mechanical, thermal, electronic and optoelectronics properties of BaMoO4 with oxygen vacancy by ab-initio calculations, Mater Today Commun. 34 (2023) 105074. https://doi.org/10.1016/J.MTCOMM.2022.105074.

[59] H. Gao, S. Wang, Y. Wang, H. Yang, L. Fang, X. Chen, Z. Yi, D. Li, Fabrication and Characterization of BaMoO4-Coupled CaWO4 Heterojunction Micro/Nanocomposites with Enhanced Photocatalytic Activity Towards MB and CIP Degradation, J Electron Mater. 51 (2022) 5230–5245. https://doi.org/10.1007/S11664-022-09769-3/FIGURES/10.

[60] Y. Wang, H. Gao, S. Wang, L. Fang, X. Chen, C. Yu, S. Tang, H. Liu, Z. Yi, H. Yang, Facile synthesis of BaMoO4 and BaMoO4/BaWO4 heterostructures with type -I band arrangement and enhanced photoluminescence properties, Advanced Powder Technology. 32 (2021) 4186–4197. https://doi.org/10.1016/J.APT.2021.09.028.

[61] O.M. Baby, S. Balamurugan, S.A. Ashika, T.K.S. Fathima, Synthesis and characterization of high NIR reflecting eco-friendly BaMoO4 pigments in scheelite family, Emergent Mater. 5 (2022) 1213–1225. https://doi.org/10.1007/S42247-021-00345-9/FIGURES/9.

[62] F. Izumi, K. Momma, Three-Dimensional Visualization in Powder Diffraction, Solid State Phenomena. 130 (2007) 15–20. https://doi.org/10.4028/WWW.SCIENTIFIC.NET/SSP.130.15.

[63] J.C. Sczancoski, L.S. Cavalcante, N.L. Marana, R.O. da Silva, R.L. Tranquilin, M.R. Joya, P.S. Pizani, J.A. Varela, J.R. Sambrano, M. Siu Li, E. Longo, J. Andrés, Electronic structure and optical properties of BaMoO4 powders, Current Applied Physics. 10 (2010) 614–624. https://doi.org/10.1016/J.CAP.2009.08.006.

[64] M.R.D. Bomio, R.L. Tranquilin, F. V. Motta, C.A. Paskocimas, R.M. Nascimento, L. Gracia, J. Andres, E. Longo, Toward understanding the photocatalytic activity of PbMoO4 powders with predominant (111), (100), (011), and (110) facets. A combined experimental and theoretical study, Journal of Physical Chemistry C. 117 (2013) 21382–21395. https://doi.org/10.1021/JP407416H/SUPPL_FILE/JP407416H_SI_001.PDF.

[65] A. Azzouzi, M. Benchikhi, R. El Ouatib, Room-temperature co-precipitation synthesis of (Ca,Sr,Ba)WO4 solid solutions: Structural refinement, morphology and band gap tuning, Ceram Int. 46 (2020) 23706–23718. https://doi.org/10.1016/J.CERAMINT.2020.06.144.

[66] S.K. Ray, Y.K. Kshetri, D. Dhakal, C. Regmi, S.W. Lee, Photocatalytic degradation of Rhodamine B and Ibuprofen with upconversion luminescence in Ag-BaMoO4: Er3+/Yb3+/K+ microcrystals, J Photochem Photobiol A Chem. 339 (2017) 36–48. https://doi.org/10.1016/J.JPHOTOCHEM.2017.02.014.

[67] S.K. Ray, D. Dhakal, R.P. Pandey, S.W. Lee, Ag-BaMoO4: Er3+/Yb3+ photocatalyst for antibacterial application, Materials Science and Engineering: C. 78 (2017) 1164–1171. https://doi.org/10.1016/J.MSEC.2017.04.115.

[68] D. Guo, Q. Yang, H. Hua, C. Hu, Room temperature ferromagnetism in shuttle-like BaMoO4 microcrystals, Journal of Physical Chemistry C. 118 (2014) 13826–13832. https://doi.org/10.1021/JP504429G/ASSET/IMAGES/LARGE/JP-2014-04429G_0010.JPEG.

[69] X. Guo, Q. Zhang, T. Liu, M. Song, J. Yin, H. Zhang, X. Wang, First-principles study on electronic structures of BaMoO4 crystals containing F and F+ color centers, Nucl Instrum Methods Phys Res B. 267 (2009) 1093–1096. https://doi.org/10.1016/J.NIMB.2009.01.013.

[70] L.S. Cavalcante, J.C. Sczancoski, R.L. Tranquilin, M.R. Joya, P.S. Pizani, J.A. Varela, E. Longo, BaMoO4 powders processed in domestic microwave-hydrothermal: Synthesis, characterization and photoluminescence at room temperature, Journal of Physics and Chemistry of Solids. 69 (2008) 2674–2680. https://doi.org/10.1016/J.JPCS.2008.06.107.

[71] F.A. Kröger, H.J. Vink, Relations between the Concentrations of Imperfections in Crystalline Solids, Solid State Physics - Advances in Research and Applications. 3 (1956) 307–435. https://doi.org/10.1016/S0081-1947(08)60135-6.

[72] R. Hoppe, Effective coordination numbers (ECoN) and mean fictive ionic radii (MEFIR), Z Kristallogr Cryst Mater. 150 (1979) 23–52. https://doi.org/10.1524/ZKRI.1979.150.14.23.

[73] R.F.P. Nogueira, W.F. Jardim, A fotocatálise heterogênea e sua aplicação ambiental, Quim Nova. 21 (1998) 69–72. https://doi.org/10.1590/S0100-40421998000100011.

[74] J. Zhang, W. Yu, J. Liu, B. Liu, Illustration of high-active Ag 2 CrO 4 photocatalyst from the first-principle calculation of electronic structures and carrier effective mass, in: Appl Surf Sci, Elsevier B.V., 2015: pp. 457–462. https://doi.org/10.1016/j.apsusc.2015.08.084.

[75] J. Low, S. Cao, J. Yu, S. Wageh, Two-dimensional layered composite photocatalysts, Chemical Communications. 50 (2014) 10768–10777. https://doi.org/10.1039/c4cc02553a.

[76] H. Zhang, L. Liu, Z. Zhou, Towards better photocatalysts: First-principles studies of the alloying effects on the photocatalytic activities of bismuth oxyhalides under visible light, Physical Chemistry Chemical Physics. 14 (2012) 1286–1292. https://doi.org/10.1039/c1cp23516h.

[77] F. Mondaca, F.A. Calderón, S. Conejeros, A.I. Mtz-Enriquez, The optoelectronic properties of Eu/F-codoped tin oxide, an experimental and DFT study, Ceram Int. 47 (2021) 31756–31764. https://doi.org/10.1016/J.CERAMINT.2021.08.057.

[78] T. le Bahers, M. Rérat, P. Sautet, Semiconductors used in photovoltaic and photocatalytic devices: Assessing fundamental properties from DFT, Journal of Physical Chemistry C. 118 (2014) 5997–6008. https://doi.org/10.1021/jp409724c.

[79] J. Ravichandran, W. Siemons, M.L. Scullin, S. Mukerjee, M. Huijben, J.E. Moore, A. Majumdar, R. Ramesh, Tuning the electronic effective mass in double-doped SrTiO3, Phys Rev B Condens Matter Mater Phys. 83 (2011). https://doi.org/10.1103/PhysRevB.83.035101.

[80] A.M. Huerta-Flores, I. Juárez-Ramírez, L.M. Torres-Martínez, J.E. Carrera-Crespo, T. Gómez-Bustamante, O. Sarabia-Ramos, Synthesis of AMoO4 (A = Ca, Sr, Ba) photocatalysts and their potential application for hydrogen evolution and the degradation of tetracycline in water, J Photochem Photobiol A Chem. 356 (2018) 29–37. https://doi.org/10.1016/j.jphotochem.2017.12.029.

[81] B.K. Maji, H. Jena, R. Asuvathraman, K.V.G. Kutty, Electrical conductivity and thermal expansion behavior of MMoO4 (M = Ca, Sr and Ba), J Alloys Compd. 640 (2015) 475–479. https://doi.org/10.1016/J.JALLCOM.2015.04.054.

[82] S.K. Ray, J. Hur, Surface modifications, perspectives, and challenges of scheelite metal molybdate photocatalysts for removal of organic pollutants in wastewater, Ceram Int. 46 (2020) 20608–20622. https://doi.org/10.1016/J.CERAMINT.2020.05.245.

[83] Y. Liang, M. Ding, Y. Yang, K. Xu, X. Luo, T. Yu, W. Zhang, W. Liu, C. Yuan, Highly dispersed Pt nanoparticles on hierarchical titania nanoflowers with {010} facets for gas sensing and photocatalysis, J Mater Sci. 54 (2019) 6826–6840. https://doi.org/10.1007/S10853-019-03379-X/TABLES/2.

[84] N. V. Lebukhova, N.F. Karpovich, Carbothermic reduction of cobalt and nickel tungstates, Inorganic Materials 2006 42:3. 42 (2006) 310–315. https://doi.org/10.1134/S0020168506030174.

[85] Z. Luo, H. Li, H. Shu, K. Wang, J. Xia, Y. Yan, Synthesis of BaMoO4 nestlike nanostructures under a new growth mechanism, Cryst Growth Des. 8 (2008) 2275–2281. https://doi.org/10.1021/CG700967Y/ASSET/IMAGES/LARGE/CG-2007-00967Y_0004.JPEG.

[86] L.S. Cavalcante, J.C. Sczancoski, R.L. Tranquilin, J.A. Varela, E. Longo, M.O. Orlandi, Growth mechanism of octahedron-like BaMoO4 microcrystals processed in microwave-hydrothermal: Experimental observations and computational modeling, Particuology. 7 (2009) 353–362. https://doi.org/10.1016/J.PARTIC.2009.05.002.

[87] V.S. Marques, L.S. Cavalcante, J.C. Sczancoski, A.F.P. Alcântara, M.O. Orlandi, E. Moraes, E. Longo, J.A. Varela, M. Siu Li, M.R.M.C. Santos, Effect of different solvent ratios (water/ethylene glycol) on the growth process of CaMoO4 crystals and their optical properties, Cryst Growth Des. 10 (2010) 4752–4768. https://doi.org/10.1021/CG100584B/SUPPL_FILE/CG100584B_SI_001.PDF.

[88] X. Wu, J. Du, H. Li, M. Zhang, B. Xi, H. Fan, Y. Zhu, Y. Qian, Aqueous mineralization process to synthesize uniform shuttle-like BaMoO4 microcrystals at room temperature, J Solid State Chem. 180 (2007) 3288–3295. https://doi.org/10.1016/J.JSSC.2007.07.010.

[89] M. Dasog, G.B. De Los Reyes, L. V. Titova, F.A. Hegmann, J.G.C. Veinot, Size vs Surface: Tuning the Photoluminescence of Freestanding Silicon Nanocrystals Across the Visible Spectrum via Surface Groups, ACS Nano. 8 (2014) 9636–9648. https://doi.org/10.1021/NN504109A/SUPPL_FILE/NN504109A_SI_001.PDF.

[90] J. Wang, C. Zheng, J. Ning, L. Zhang, W. Li, Z. Ni, Y. Chen, J. Wang, S. Xu, Luminescence signature of free exciton dissociation and liberated electron transfer across the junction of graphene/GaN hybrid structure, Scientific Reports 2015 5:1. 5 (2015) 1–6. https://doi.org/10.1038/srep07687.

[91] W. Lu, Y. Ou, E.M. Fiordaliso, Y. Iwasa, V. Jokubavicius, M. Syväjärvi, S. Kamiyama, P.M. Petersen, H. Ou, White Light Emission from Fluorescent SiC with Porous Surface, Scientific Reports 2017 7:1. 7 (2017) 1–9. https://doi.org/10.1038/s41598-017-10771-7.

[92] T.L. Rittenhouse, P.W. Bohn, T.K. Hossain, I. Adesida, J. Lindesay, A. Marcus, Surface-state origin for the blueshifted emission in anodically etched porous silicon carbide, J Appl Phys. 95 (2004) 490–496. https://doi.org/10.1063/1.1634369.

[93] Y. Sun, J. Ma, J. Fang, C. Gao, Z. Liu, Synthesis of BaMoO4 high photoluminescent whiskers by an electrochemical method, Ceram Int. 37 (2011) 683–686. https://doi.org/10.1016/J.CERAMINT.2010.09.052.

[94] S.K. Ray, J. Hur, Surface modifications, perspectives, and challenges of scheelite metal molybdate photocatalysts for removal of organic pollutants in wastewater, Ceram Int. 46 (2020) 20608–20622. https://doi.org/10.1016/j.ceramint.2020.05.245.

[95] G.S. Kamble, Y.C. Ling, Solvothermal synthesis of facet-dependent BiVO4 photocatalyst with enhanced visible-light-driven photocatalytic degradation of organic pollutant: assessment of toxicity by zebrafish embryo, Sci Rep. 10 (2020). https://doi.org/10.1038/s41598-020-69706-4.

[96] M.C. Toroker, D.K. Kanan, N. Alidoust, L.Y. Isseroff, P. Liao, E.A. Carter, First principles scheme to evaluate band edge positions in potential transition metal oxide photocatalysts and photoelectrodes, Physical Chemistry Chemical Physics. 13 (2011) 16644–16654. https://doi.org/10.1039/C1CP22128K.

[97] G. Yanalak, A. Ozen, A. Sarılmaz, A. Keles, E. Aslan, F. Ozel, I. Hatay Patir, Scheelite-type BaMoO4 and BaWO4 based dye sensitized photocatalytic hydrogen evolution by water splitting, Journal of Physics and Chemistry of Solids. 168 (2022) 110821. https://doi.org/10.1016/J.JPCS.2022.110821.

Graphical abstract

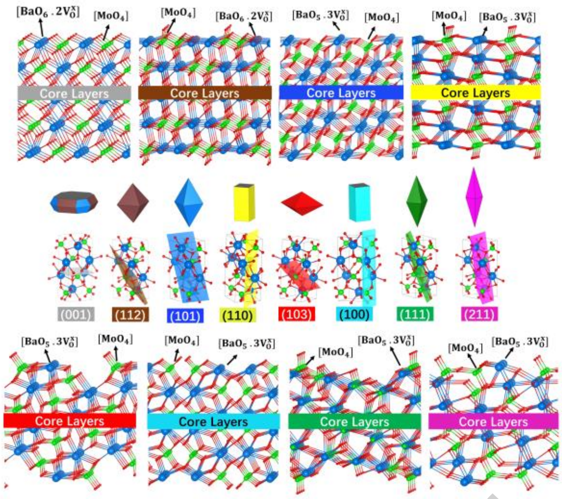

Credit author statement

José A. S. Laranjeira: Conceptualization, Methodology, Software, Validation, Formal analysis, Investigation, Writing - Original Draft, Writing - Review & Editing. **Sérgio A. Azevedo:** Conceptualization, Methodology, Software, Validation, Formal analysis, Investigation, Writing - Original Draft, Writing - Review & Editing. **Nicolas F. Martins:** Data Curation, Validation, Visualization, Writing - Review & Editing. **Felipe A. La Porta:** Conceptualization, Methodology, Validation, Data Curation, Visualization, Writing - Review & Editing. **Elson Longo:** Conceptualization, Validation, Visualization, Funding acquisition, Writing - Review & Editing. **Julio R. Sambrano:** Conceptualization, Validation, Visualization, Supervision, Project administration, Funding acquisition, Writing - Review & Editing.

Declaration of interests

☒The authors declare that they have no known competing financial interests or personal relationships that could have appeared to influence the work reported in this paper.

☐The authors declare the following financial interests/personal relationships which may be considered as potential competing interests: